

Boundary geometry controls a topological defect transition that determines lumen nucleation in embryonic development

Pamela C. Guruciaga,^{1,2,*} Takafumi Ichikawa,^{3,4} Takashi Hiiragi,^{3,4,5,†} and Anna Erzberger^{1,6,‡}

¹*Cell Biology and Biophysics Unit, European Molecular Biology Laboratory (EMBL), Meyerhofstraße 1, 69117 Heidelberg, Germany*

²*Developmental Biology Unit, European Molecular Biology Laboratory (EMBL), Meyerhofstraße 1, 69117 Heidelberg, Germany*

³*Institute for the Advanced Study of Human Biology (WPI-ASHBi), Kyoto University, Kyoto, 606-8501, Japan*

⁴*Department of Developmental Biology, Graduate School of Medicine, Kyoto University, Kyoto, 606-8501, Japan*

⁵*Hubrecht Institute, Uppsalalaan 8, 3584 CT Utrecht, The Netherlands*

⁶*Department of Physics and Astronomy, Heidelberg University, 69120 Heidelberg, Germany*

(Dated: September 5, 2024)

Topological defects determine the collective properties of anisotropic materials. How their configurations are controlled is not well understood however, especially in 3D. In living matter moreover, 2D defects have been linked to biological functions, but the role of 3D polar defects is unclear. Combining computational and experimental approaches, we investigate how confinement geometry controls surface-aligned polar fluids, and what biological role 3D polar defects play in tissues interacting with extracellular boundaries. We discover a charge-preserving transition between 3D defect configurations driven by boundary geometry and independent of material parameters, and show that defect positions predict the locations where fluid-filled lumina—structures essential for development—form within the confined polar tissue of the mouse embryo. Experimentally perturbing embryo shape beyond the transition point, we moreover create additional lumina at predicted defect locations. Our work reveals how boundary geometry controls polar defects, and how embryos use this mechanism for shape-dependent lumen formation. We expect this defect control principle to apply broadly to systems with orientational order.

* pamela.guruciaga@embl.de

† t.hiiragi@hubrecht.eu

‡ erzberge@embl.de

Confinement plays a fundamental role in directing self-organisation [1] in various contexts including colloids [2], developing tissues [3, 4], liquid crystals [5], and crowds of people [6]. Controlling confining structures and predicting their impact on the collective properties of the confined bulk will reveal organisational principles of complex systems like living matter [7] and enable technological applications such as the design of optoelectronic [8] and microfluidic [9] devices. Boundary effects are especially relevant for materials comprised of anisotropic particles, which possess orientational degrees of freedom and tend to align with their neighbours. In liquid crystals, for example, substrates with particular surface topography or chemical functionality [10] induce the alignment of adjacent molecules, creating an ordered layer that propagates into the bulk by elastic forces. In this way, surface-induced alignment allows to achieve different desired configurations of the order parameter (OP) by tuning the boundary conditions, for example in nematics [11–13]. However, the effects of boundary geometry on the bulk organisation of anisotropic materials is not well understood, particularly for curved surfaces in 3D.

Confinement also influences the internal organisation of living materials, e.g. how multicellular systems undergo morphogenesis in biofilms [14] or during embryonic development [15]. The boundary interactions between anisotropic living matter such as tissues consisting of polarised cells, and extracellular matrix (ECM) involve diverse biophysical processes, including adhesion and polarity signaling [16–18], which affect ordering at the collective scale similar to boundary-induced alignment. For instance, basement membrane layers promote specific orientations of adjacent cells for different types of polarity—parallel for epithelial planar [19, 20] and mesenchymal/migratory polarity [21–23], and perpendicular for apico-basal epithelial polarity [24]. Coherent apico-basal alignment is crucial for epithelial functions such as molecule transport across the tissue, and is linked to the formation of fluid-filled cavities (lumina) [24]. Orientational boundary effects could provide general mechanisms by which confining structures control multicellular organisation.

Many collective properties of ordered materials depend on the number and spatial distribution of topological defects, i.e. points in the OP field where the orientation is not defined. In the case of nematic systems confined to a surface, geometric constraints have been shown to play an important role in determining defect configurations and dynamics [25, 26]. In biological contexts, defects can guide diverse cellular processes [27] and have been shown to trigger the formation of structures such as fruiting bodies [28] and tentacles [29]. However, despite their potential biological role, 3D polar defects and their relation to system geometry remain unexplored, with most investigations focusing on 2D domains and nematic systems, applicable in multicellular contexts where cells can be approximated as elongated units. These approaches have successfully predicted the collective dynamics of bacterial colonies [28, 30, 31], cell populations [25, 32], and epithelial sheets [33, 34]. However, in contexts where cellular polarity implies distinct sub-cellular regions with specific functions—such as mesenchymal collective cell migration [35, 36]—, the polar nature of cells is relevant for understanding collective properties.

Here, we investigate how boundary effects lead to a surface–bulk coupling that permits controlling the properties of anisotropic materials through confining geometry. Specifically, we analyse how the mechanical properties and geometry of the boundaries drive the ordering of a 3D polar fluid, and we identify three transitions in which defects in the bulk OP field appear out of a uniform field, or change their configuration. We also study the role of boundary geometry on the bulk organisation of polarised cells, using the mouse epiblast—the tissue that forms the embryo proper during

development—as an example. Orientational order of apico-basal polarity in the epiblast is linked to the formation of a central lumen, a critical event in normal mouse development [37, 38]. By associating the polar OP field with the local average cellular apico-basal polarity in the tissue, we find that 3D-field defect configurations are parameter-free predictors of lumen initiation sites. Moreover, using a recently developed *ex vivo* culturing approach [37], we experimentally perturb epiblast boundary shape to induce additional lumen nucleation sites at the predicted positions.

WEAK BOUNDARY-INDUCED ALIGNMENT IN A 3D POLAR FLUID

A polar fluid in a 3D space Ω with volume V_0 is characterised by a 3D vector OP $\mathbf{p}(\mathbf{r})$. This local quantity represents the average polarity of particles in a volume element [39], and defines the global degree of order

$$P \equiv \langle |\mathbf{p}| \rangle_\Omega = \frac{1}{V_0} \int_\Omega dV |\mathbf{p}|. \quad (1)$$

The free energy functional of such a system is

$$\mathcal{F}[\mathbf{p}] = \int_\Omega dV f_B(\mathbf{p}, \nabla \mathbf{p}) + \int_{\partial\Omega} dS f_S(\mathbf{p}), \quad (2)$$

where f_B and f_S are the bulk and surface energy densities. We minimise equation (2) with respect to OP variations and impose boundary conditions

$$\frac{\partial f_S}{\partial p_i} + \hat{\mathbf{n}} \cdot \frac{\partial f_B}{\partial (\nabla p_i)} = 0 \quad \text{in } \partial\Omega, \quad (3)$$

where $\hat{\mathbf{n}}$ is the outward normal, to obtain the Euler–Lagrange equations for the three components p_i (see [Supplementary note](#))

$$\frac{\partial f_B}{\partial p_i} - \nabla \cdot \frac{\partial f_B}{\partial (\nabla p_i)} = 0 \quad \text{in } \Omega. \quad (4)$$

Equations (3) ensure continuity of the OP on the boundary, coupling it to its bulk value.

Following the Landau–de Gennes approach to the nematic–isotropic transition in liquid crystals [40], we write the bulk energy density as $f_B = f_R + f_E$. To focus on boundary-induced order, we consider a restoring term $f_R = a|\mathbf{p}|^2/2$ with $a \gtrsim 0$ favouring the disordered state $\mathbf{p} = 0$. The second term is given by the elastic contribution

$$f_E = \frac{k_0}{2} (\nabla \cdot \mathbf{p})^2 + \frac{k_1}{2} [\hat{\mathbf{p}} \cdot (\nabla \times \mathbf{p})]^2 + \frac{k_2}{2} [\hat{\mathbf{p}} \times (\nabla \times \mathbf{p})]^2 \quad (5)$$

with $\hat{\mathbf{p}} = \mathbf{p}/|\mathbf{p}|$, in which we do not impose the one-constant approximation for the coefficients k_0, k_1, k_2 that penalise splay, twist, and bend distortions. Note that the coupling between the magnitude and orientational degrees of freedom in Eq. (5) produces a regularizing cross-term absent in the classical Frank free energy.

The surface energy density f_S represents a weak anchoring interaction between the fluid and the confining surface $\partial\Omega$ [41–43], where the OP at the boundary is not fixed as in the strong case [11–13, 44]. Deviations from the *preferred value* \mathbf{p}_0 at the surface are penalised as [42, 45]

$$f_S = \frac{w}{2} (\mathbf{p} - \mathbf{p}_0)^2. \quad (6)$$

The constant $w > 0$ defines the anchoring length $\lambda \equiv w/a$. Surface anchoring is known to control the defect structure in liquid crystals in the nematic phase [5, 44, 46]. In spherical confinement, a homeotropic boundary condition produces a radial defect in the centre, while a tangential alignment favours the appearance of two surface defects (boojums) at the poles. For a polar OP, however, several tangential orientations are possible, and mixed boundary conditions—with both tangential and normal \mathbf{p}_0 —remain unexplored, although a related problem was studied for liquid crystals in Ref. [44].

MATERIAL PARAMETERS DETERMINE THE CREATION OF 3D POLAR DEFECTS

Mixed boundary conditions are relevant whenever a polar material contacts surfaces with different properties. For example, the mouse epiblast at embryonic day 5 is confined by two interfaces: an approximately hemispherical ECM layer promoting perpendicular alignment of epiblast apico-basal polarity via biochemical and mechanical processes [37, 47], and a less curved tissue–tissue interface with the extra-embryonic ectoderm, to which cells orient predominantly parallel (Fig. 1). To investigate how these non-uniform boundaries favouring distinct distortion modes affect bulk organisation, we analyse the impact of different elastic coefficients [48, 49]. Given that lateral interactions dominate in apico-basally polarised cells [24], we expect splay distortions to be most significant. Numerical minimisation of equation (2) in spherical confinement with tangential and mixed \mathbf{p}_0 reveals distinct field configurations and defect structures based on the elastic constant ratio k_0/k_2 (Fig. 2a-b, see Methods). Note that the twist contribution vanishes by symmetry. While there are only surface defects for $k_0/k_2 = 1$, bulk defects form and move away from the surface as the ratio k_0/k_2 increases (Fig. 2c), similar to the transition between nematic tactoids and toroids [49]. The type of bulk defects depends on the preferred orientation on the surface, with pole-to-pole tangential \mathbf{p}_0 giving rise in the $k_0 \gg k_2$ limit to a toroidal vortex tube centred on the symmetry axis resembling the flow lines of a passive fluid in contact with an active surface [50]. In contrast, the combination of tangential and normal preferred orientations results in a configuration with a hyperbolic point defect on the symmetry axis accompanied by a radial disclination ring around it.

In the following, we focus on the splay-dominated regime, and define the correlation length of the material $\xi \equiv \sqrt{k_0/a}$. While the development of global order is promoted by the surface anchoring (and modulated by the surface–to–volume ratio, see Extended Data Fig. 1a), the correlation length determines the penetration of boundary-induced order into the bulk ($\xi > \xi^* \approx 0.4R_0$ for a sphere, Fig. 2d). The extrapolation length $\zeta \equiv k_0/w = \xi^2/\lambda$ sets the relative importance of bulk versus boundary interactions. Defects appear when surface anchoring dominates over the bulk $\zeta < \zeta^* \approx 0.3R_0$, trading off the cost of bulk distortions in favour of better alignment with the preferred orientations at the boundaries, comparable to the transition in nematic tactoids [41]. We find that the number and structure of defects depend on the confinement geometry. While in both spherical and hemispherical confinement a pair of radial (rad+1) and negative hyperbolic (hyp−1) hedgehogs nucleate at the transition, in the former the rad+1 defect further decomposes into a positive hyperbolic (hyp+1) hedgehog and radial disclination ring (r-ring) on increasing anchoring (Figs. 2d-e, Extended Data Figs. 1a-b). The topological charge for both geometries changes from neutral to +1 when the hyp−1 hedgehog moves up and becomes a hyperbolic boojum [51] on the cap surface (Fig. 2e, Extended

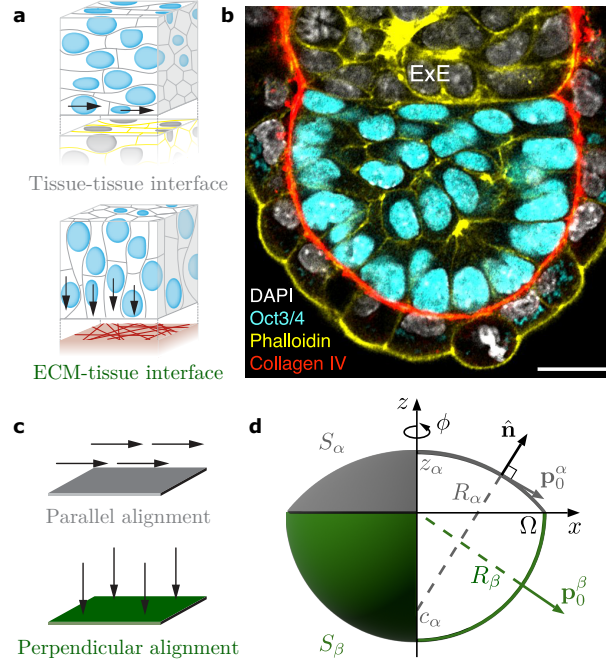


FIG. 1. **Multicellular interactions and boundary-induced alignment.** **a**, Apico-basally polarised cells tend to align parallel to a tissue–tissue interface (top) and perpendicular to a tissue–ECM interface (bottom), similar to an anchoring effect [equation (6)]. **b**, Immunofluorescence image stained for an ECM component (Collagen IV), actin (Phalloidin), an epiblast marker (Oct3/4), and DNA (DAPI) shows the central cross-section of a representative mouse embryo after *ex vivo* culture for 18 hours from embryonic day 4.5. At this stage, the epiblast consists of apico-basally polarised cells (cyan nuclei) in contact with a cup-shaped ECM layer (red) and a tissue–tissue interface with the extra-embryonic ectoderm (ExE). Scale bar 20 μm . Adapted from Ref. [37]. **c**, We consider two types of surfaces that favour parallel (gray) or perpendicular (green) preferred orientations \mathbf{p}_0 in a contacting polar fluid, similar to the cell–boundary interactions at tissue–tissue and tissue–ECM interfaces. **d**, We parameterize the epiblast-like class of acorn shapes with $\nu \equiv z_\alpha/R_\beta$. The base S_β is defined as a hemisphere with radius R_β centred at the origin of coordinates, while the spherical cap S_α has radius R_α , centre $(0, c_\alpha)$ on the symmetry axis, and maximum height z_α . Vectors \mathbf{p}_0^α and \mathbf{p}_0^β depict the mixed preferred orientation on the boundary.

Data Fig. 1b). Note that the r-ring carries no charge [52]. Hereafter, we concentrate on the surface-dominated, defect-containing regime ($\zeta \ll \zeta^*$).

BOUNDARY SHAPE CONTROLS CHARGE-PRESERVING DEFECT TRANSITIONS

Motivated by the shape of the mouse epiblast, we systematically examine the role of boundary geometry on 3D polar OP field configurations in the family of axis-symmetric *acorn* shapes, whose geometry is fully parameterized by $\nu \equiv z_\alpha/R_\beta$ with z_α the maximum height of the spherical-shell cap and R_β the radius of the hemispherical base (Fig. 1d, see Methods). While $\nu = 0$ corresponds to a flat tissue–tissue interface, $0 < \nu \leq 1$ (respectively $-1 < \nu < 0$) represent convex (respectively concave) interfaces, with $\nu = 1$ the spherical case. The total volume V_0 is fixed and defines a length scale $R_0 \equiv (3V_0/4\pi)^{1/3}$.

Fixing the material length scales in the splay- and surface-dominated regime, we vary the acorn parameter ν

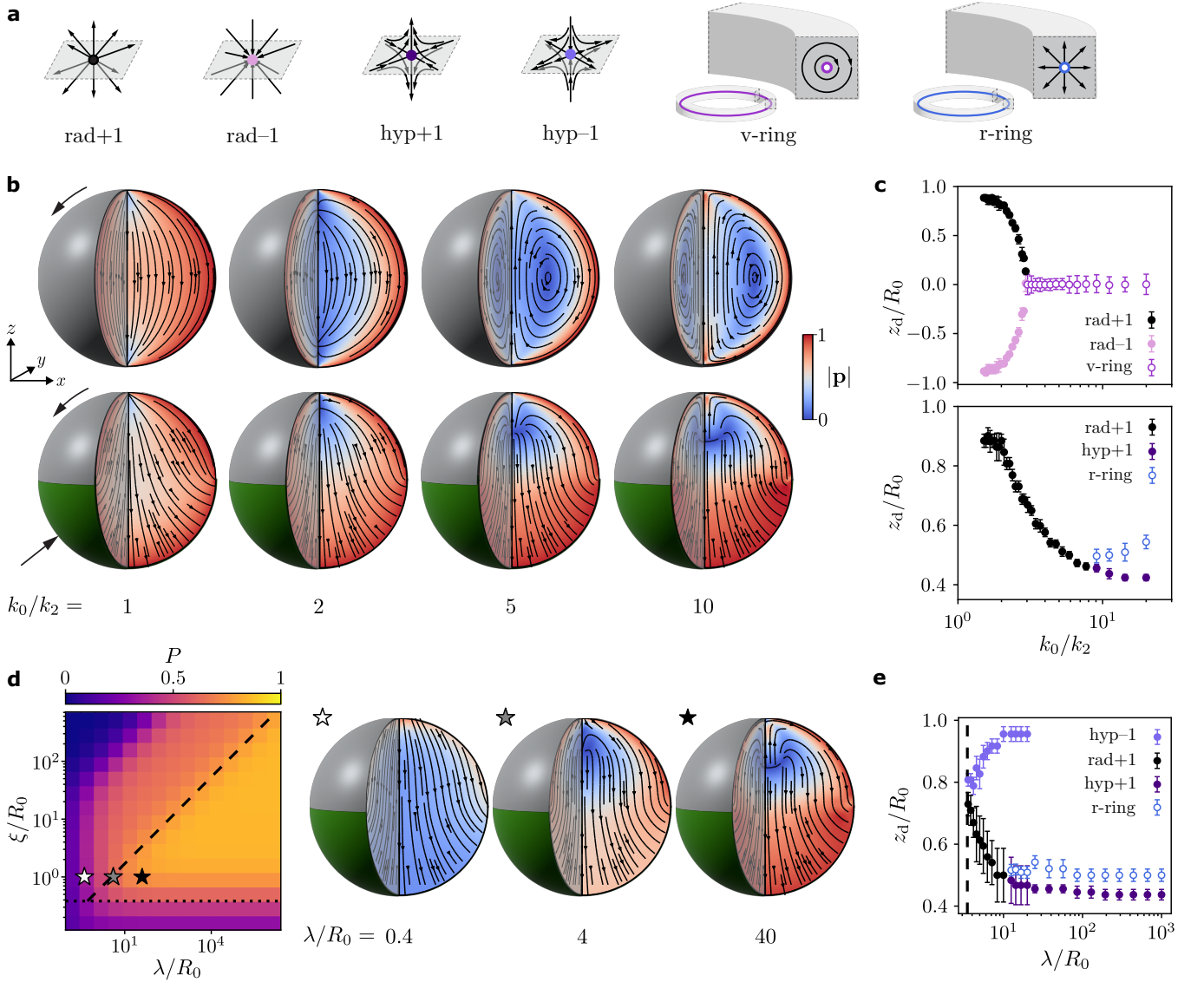


FIG. 2. Material parameters determine the creation of 3D polar defects. **a**, Polar systems in 3D feature diverse defect structures. Schematics show the configurations of the radial +1 (black), radial -1 (pink), hyperbolic +1 (purple), hyperbolic -1 (lilac) hedgehogs, and the vortex (empty magenta) and radial (empty blue) disclination rings. **b**, Streamlines and colour map show the local direction and magnitude of the equilibrium OP field for $\lambda/R_0 = 100$ and $\xi/R_0 = 1$ in spherical confinement with varying k_0/k_2 for uniform (top) and mixed (bottom) boundaries. External arrows denote \mathbf{p}_0 on parallel-aligning (gray) and perpendicular-aligning (green) surfaces. **c**, Bulk defects are created and change their height z_d as the system becomes splay-dominated ($\lambda/R_0 = 100$, $\xi/R_0 = 1$). The type and quantity of defects depends on the boundary preference (top: uniform, bottom: mixed). **d**, Global degree of order P [equation (1)] for a sphere with mixed \mathbf{p}_0 . For $\xi < \xi^* \approx 0.4R_0$ (dotted line), the system remains disordered (i.e., $P < 0.5$) even in the limit $\lambda \rightarrow \infty$. Stars denote the parameter values for example field configurations, where pairs of defects are created in order to accommodate the increasingly relevant boundary conditions ($\xi/R_0 = 1$, $k_0/k_2 = 10$). The value $\zeta^* \approx 0.3R_0$ (dashed line) separates defect-free and defect-containing configurations. **e**, Increasing the anchoring length λ changes the defect height z_d ($\xi/R_0 = 1$, $k_0/k_2 = 10$). The hyp-1 bulk defect moves up and becomes a hyperbolic boojum on the surface, while the rad+1 decomposes into a combination of a hyp+1 and a r-ring. Their positions and the global degree of order P reach a plateau as $\lambda \rightarrow \infty$. Points and error bars correspond to the mean and standard deviation of the position of the defect candidates (see Methods). The vertical dashed line marks the value $\lambda^* = \xi^2/\zeta^*$.

(Figs. 3a-b), and find that the defect configuration undergoes a transition from radial hedgehog to a combination of hyp+1 point defect plus r-ring at ν_c^+ and ν_c^- . Notably, the surface-to-volume ratio and the global degree of order P (Fig. 3c) differ distinctly at these critical values. Measuring the position of the defects (Fig. 3b) shows that their height grows approximately linearly with the acorn parameter, and that the r-ring is nucleated with a finite radius. This renders the transitions discontinuous, comparable to the first-order transition studied in Ref. [53] in a nematic system with strong homeotropic boundary conditions. minimisations over intervals $\lambda/R_0 \in [10^2, 10^6]$ and $\xi/R_0 \in [\xi^*, \sqrt{\lambda\xi^*})/R_0$ reveal that the transition points and the position of the defects are robust to changes in material properties (Fig. 3b and Extended Data Fig. 2): the transition from the radial hedgehog to the hyp+1 and r-ring defects occurs independently of the material parameters at $\nu_c^+ = 0.400 \pm 0.008$ and $\nu_c^- = -0.54 \pm 0.09$, and the r-ring radius changes only 2-fold over an almost three orders of magnitude variation in ξ . In summary, we report a geometry-controlled transition in the defect structure of a boundary-aligned polar fluid, and show that defect locations are robust to changes in the material length scales.

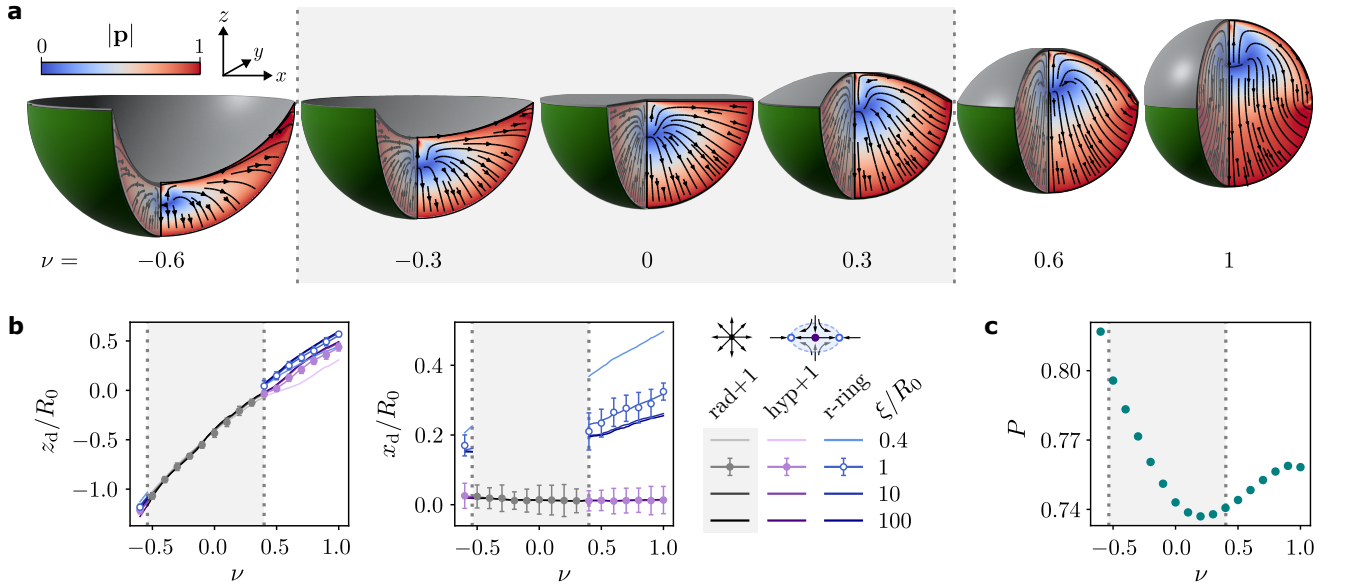


FIG. 3. Confining geometry controls charge-preserving transitions between different defect configurations. **a**, The OP fields for different shapes ν at fixed material length scales $\lambda/R_0 = 10^6$ and $\xi/R_0 = 1$ (i.e., in the highly ordered, defect-containing regime) with $k_0/k_2 = 10$ show transitions between a radial hedgehog, and a hyp+1 defect surrounded by a disclination ring. **b**, The transitions occur when the shape parameter exceeds the critical values $\nu_c^+ = 0.400 \pm 0.008$ and $\nu_c^- = -0.54 \pm 0.09$ (dotted lines). The transition points are invariant to changes in the material parameters, and defect positions undergo little variation (see also Extended Data Fig. 2). Points and error bars correspond to the mean and standard deviation of the position of the defect candidates (see Methods). **c**, The global degree of order also depends on ν , but the system remains always in the highly ordered ($P > 0.5$) regime ($\lambda/R_0 = 10^6$, $\xi/R_0 = 1$, $k_0/k_2 = 10$).

POLAR DEFECTS DETERMINE SITES OF LUMEN NUCLEATION

Topological defects are known to affect macroscopic properties of the systems they inhabit [27]. In living systems, 2D nematic defects have been shown to function as organising centers for biological processes like cell extrusion [33] or out-of-plane bending during morphogenesis [54]. However, how 3D polar defects influence multicellular organisation remains unexplored. To address this question, we consider the mouse epiblast, and associate the OP \mathbf{p} with the average orientation of apico-basally polarised cells within this confined tissue. We find that small fluid-filled cavities tend to form between the cells near positions where the OP field of a correspondingly confined polar system has radial hedgehog defects (Figs. 3a and 4a). Indeed, such lumina typically form between the apical surfaces of cells, which feature distinct molecular compositions and functional properties, with vesicle trafficking or active osmolyte pumps localising asymmetrically along the apico-basal axis [55–58], and 3D polar defects mark positions where contacts between multiple apical surfaces are likely. The geometry-driven transition we identified suggests that tissue shape controls the distribution of lumen nucleation sites, implying that externally manipulating boundary geometry may permit inducing additional lumina. We expect in particular a difference in the spatial distribution and number of lumen nucleation sites between epiblasts with shapes falling within and beyond the range $\nu \in (\nu_c^-, \nu_c^+)$, with the former containing sites only close to the central symmetry axis, and the latter presenting an additional distribution at a distance similar to the radius of the disclination ring.

To test these predictions, we performed 3D-gel embedded embryo culture (see Ref. [37]), a technique that faithfully recapitulates *in utero* embryonic development while allowing for *in toto* monitoring, measurement, and manipulation. Moreover, we experimentally perturbed the shape of the epiblast, specifically the tissue–tissue interface. The curvature of this interface depends on a preceding morphogenetic event, the inward folding of the adjacent extra-embryonic ectoderm [37, 59]. Disrupting this process results in embryos with deformed interfaces between the epiblast and this extra-embryonic tissue. We obtained mouse embryos cultured for 18 hours from embryonic day 4.5, of which epiblasts presented various shapes resulting from natural variability in the control condition (Fig. 4a) or experimental manipulation (Fig. 4b) by blocking the formation of the extra-embryonic ectoderm (see Methods). Note that the epiblast tissue volume was conserved [$\bar{V}_0^{\text{exp}} \approx (2.3 \pm 0.4) \times 10^5 \mu\text{m}^3$, see Methods]. To more accurately account for the shape variations of these embryos, we consider a two-parameter family of shapes with the base also a spherical cap, defined by ν and a new parameter σ (Figs. 4a-b). Quantifying the shapes of the 16 embryos, we obtained $\nu_{\text{exp}} \in [-0.16, 0.003]$ and $\sigma_{\text{exp}} \in [0.68, 1.43]$ for control embryos ($N = 6$; Fig. 4a, Extended Data Fig. 3), and $\nu_{\text{exp}} \in [0.69, 1.23]$ and $\sigma_{\text{exp}} \in [1.59, 2.41]$ for embryos with a morphogenetic perturbation ($N = 10$; Fig. 4b, Extended Data Fig. 3). We excluded from this analysis embryos which did not undergo elongation of the whole embryo along the distal-proximal axis or did not reach the epiblast cell number of 50 [37]. We also discarded one embryo in which the epiblast–ECM interface was concave and hence incompatible with our family of shapes. We estimated the positions of lumen initiation sites using immunostaining against apical surface components and identified single sites near the central axis in embryos with $\nu_c^- < \nu < \nu_c^+$, and additional sites as predicted for the majority of embryos with $\nu > \nu_c^+$ (Fig. 4c). Importantly, the defect positions in the OP field for the average shape of control and manipulated embryos predict the average nucleation sites in each group quantitatively (Figs. 4d and 4e). Taken together, these results show

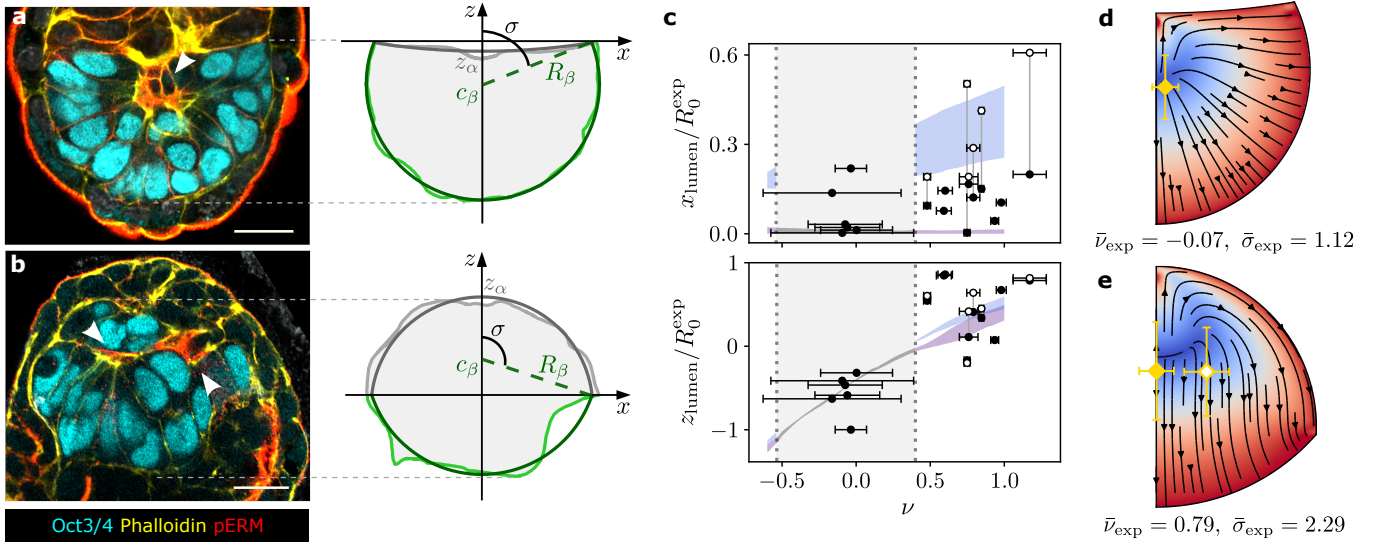


FIG. 4. **Defect positions correspond to sites of lumen nucleation in the mouse epiblast.** **a-b**, Representative immunostaining images show the central cross-section of a control (**a**) and a shape-manipulated (**b**) mouse embryo developed *ex vivo* for 18 hours from embryonic day 4.5, stained for an apical surface marker (pERM), actin (Phalloidin), and an epiblast marker (Oct3/4). Lumen initiation sites are highlighted with white arrowheads. Scale bars 20 μm . To quantify the boundary shapes, we fit segmentations (light green: tissue–ECM boundary, light gray: tissue–tissue boundary) with a combination of two spherical caps, where the base is centered at $(0, c_\beta)$. This generalised acorn family is parameterised by $\sigma \equiv \cos^{-1}(-c_\beta/R_\beta)$ and $\nu \equiv z_\alpha/R_\beta$. **c**, Lumen centroid positions plotted against individually fitted ν_{exp} show that control embryos ($N = 6$) with shapes $\nu \in (\nu_c^-, \nu_c^+)$ (shaded region between dotted lines) contain single lumina, whereas 6 out of 10 embryos with shapes perturbed beyond the transition point present additional sites (empty points; vertical lines connect lumina from the same embryo). Coloured shaded regions show the defect position ranges for ideal acorns with $\lambda/R_0 = 10^6$, $\xi/R_0 \in [0.4, 100]$ and $k_0/k_2 = 10$ as in Fig. 3b. The volume V_0^{exp} of the epiblast tissue defines $R_0^{\text{exp}} = (3V_0^{\text{exp}}/4\pi)^{1/3}$ for each embryo. Error bars are determined by residual bootstrapping of the epiblast boundaries (see [Methods](#)). **d-e**, The average lumen nucleation sites (yellow) are close to where the OP field presents defects for the average shape of control (**d**) and manipulated (**e**) epiblasts ($\xi/R_0 = 1$, $\lambda/R_0 = 10^6$, $k_0/k_2 = 10$). Error bars denote the standard deviation.

that lumina nucleate near polar defect positions and that external manipulation of embryo shape induces the creation of additional nucleation sites near the position predicted by the geometry-driven defect transition we identified.

DISCUSSION AND OUTLOOK

Confinement and boundary effects impact the bulk organisation of complex materials. We show how interactions with confining surfaces drives the creation of different topological defects in a polar fluid, and identify distinct roles for the confining geometry and bulk and surface mechanical parameters: while the competition between bulk distortion and surface anchoring governs the transition between defect-free and defect-containing states, the *types* of defects observed and the transitions between different defect configurations depend solely on the geometry. Moreover, in the surface-dominated regime, 3D defect positions are robust against anchoring and correlation length variations. We thus report a novel, charge-preserving defect transition controlled by confining geometry.

In living systems, the impact of topological defects on macroscopic spatial organisation is not limited to distortion effects; they can also localise regulatory molecules that drive subsequent biological processes [27]. Examples include the activation of cell–death signals leading to cell extrusion [33], or assembling organisational centres during morphogenesis [54, 60]. For the mouse epiblast—a tissue consisting of apico-basally polarised cells—we find that defects guide the formation of fluid-filled cavities. Although lumina fulfill critical biological functions in tissue organisation and cell fate specification [61–63], how their spatial arrangement within a tissue arises is unclear. The molecular processes that drive lumen formation in the epiblast as well as in numerous other tissues [58], such as active osmolyte pumping, localise to structures at the apical side of cells [55, 56]. That defects mark spatial regions where apical surfaces converge and lumina nucleate is therefore likely, and we indeed found that defect positions are quantitative parameter-free predictors of lumen nucleation sites in this system. Furthermore, we accomplished inducing additional lumen nucleation sites by experimentally perturbing the boundary geometry beyond the transition point, where the correspondingly confined polar fluid presents an additional defect. That the spatial distribution of early luminal structures follows the predicted geometry-dependent changes suggests that embryo shape regulates lumen formation via orientational effects. Lumen formation might therefore serve as a shape-sensing checkpoint mechanism in the embryo, determining successful amniotic cavity development.

It will be exciting to investigate the interplay between surface-induced alignment and boundary geometry in other experimental systems to challenge the generality of this mechanism for the spatial organisation of defect-associated structures. Importantly, since defect configurations depend almost exclusively on the geometry, the relevant observables are directly accessible from imaging data. Quantitative predictions can be made without fitting of material parameters, indeed without having to make detailed assumptions about specific bulk or surface properties. This robustness not only renders experimental testing feasible, but also suggests that spatial control of defect-associated processes via boundary geometry is a general phenomenon across systems with orientational degrees of freedom, independent of scale or material specifics.

For multicellular systems, our formalism offers a general and tractable framework for studying cell–ECM interactions. Using a single anchoring parameter to capture the coupling between cellular polarity and extra-cellular materials like basement membranes will allow the investigation of the feedback between geometry changes and boundary-induced order from active ECM remodeling by cellular processes—properties distinguishing multicellular systems from passive anisotropic materials in confinement.

In conclusion, our investigations reveal how boundary geometry controls defect configurations within polar materials, and uncover a new biological function for 3D polar defects in multicellular systems. More broadly, that shape can control defect configurations independently of material specifics constitutes a general geometry-dependent organisational principle. Having demonstrated its predictive power in a system as complex and intractable as a living embryo, we expect this defect-control mechanism to be relevant in diverse orientational systems.

METHODS

Geometrical definitions

Ideal acorn

If the total volume V_0 of the system is fixed, geometrical parameters c_α , R_α and R_β (see Fig. 1d in the main text) are defined solely by $\nu \equiv z_\alpha/R_\beta$ through the system of equations

$$\begin{cases} R_\alpha^2 = R_\beta^2 + c_\alpha^2 \\ \nu R_\beta = c_\alpha + \text{sgn } \nu R_\alpha \\ V_0 = \frac{2\pi}{3} R_\beta^3 + \text{sgn } \nu \frac{\pi}{3} (R_\alpha - |c_\alpha|)^2 (2R_\alpha + |c_\alpha|) \end{cases} . \quad (7)$$

The cap S_α —representing the tissue–tissue interface—can be parameterised in spherical coordinates as $r = r_\alpha(\theta) = c_\alpha \cos \theta + \sqrt{R_\alpha^2 - c_\alpha^2 \sin^2 \theta}$ for $\theta \in [0, \pi/2]$ (respectively $\theta \in [\pi/2, \pi]$) if $\nu > 0$ (respectively $\nu < 0$). Note that this includes $\nu = 1$, since in that case $c_\alpha = 0$ and $R_\alpha = R_\beta$. If $\nu = 0$, however, S_α is given by the disk with $r \in [0, R_\beta]$ and $\theta = \pi/2$. Finally, the base S_β —corresponding to the tissue–ECM interface—is simply $r = R_\beta$ and $\theta \in [\pi/2, \pi]$ for all ν . In all cases, $\phi \in [0, 2\pi)$. With these definitions, the mixed preferred orientation in the spherical basis consists of $\mathbf{p}_0^\beta = (1, 0, 0) \forall \nu$ on S_β , and

$$\mathbf{p}_0^\alpha = \begin{cases} (1, 0, 0) & \text{if } \nu = 0 \\ (\sin \theta - \text{sgn } \nu g_\alpha(\theta) \sin \theta \cos \theta, \cos \theta + \text{sgn } \nu g_\alpha(\theta) \sin^2 \theta, 0) & \text{if } 0 < |\nu| < 1 \\ (0, 1, 0) & \text{if } \nu = 1 \end{cases} \quad (8)$$

with

$$g_\alpha(\theta) = \frac{r_\alpha(\theta)}{\sqrt{R_\alpha^2 - r_\alpha^2(\theta) \sin^2 \theta}} \quad (9)$$

on S_α . Note that the tissue–tissue interaction could in principle be modelled as nematic. However, we expect no significant difference, since the outward-normal \mathbf{p}_0^β imposed by the tissue–ECM boundary and the polar character of the constituents break this symmetry and favour the north-south orientation given by \mathbf{p}_0^α .

Generalised acorn

In a more general scenario, the base S_β of the acorn can be centred at a point $(0, c_\beta)$ different from the origin of coordinates. Such a system can be characterised by two dimensionless parameters: ν , as introduced before, and $\sigma \equiv \cos^{-1}(-c_\beta/R_\beta)$ (see Figs. 4a and 4b in the main text). Considering a constant volume V_0 , the equations that

geometrical parameters c_α , R_α , c_β and R_β must satisfy are

$$\begin{cases} R_\alpha^2 = R_\beta^2 + (c_\beta - c_\alpha)^2 + 2(c_\beta - c_\alpha)R_\beta \cos \sigma \\ \nu R_\beta = c_\alpha + \text{sgn } \nu R_\alpha \\ V_0 = \frac{\pi}{3} R_\beta^3 (2 - \cos \sigma) (1 + \cos \sigma)^2 + \nu \frac{\pi}{6} R_\beta^3 (3 \sin^2 \sigma + \nu^2) \end{cases} . \quad (10)$$

While S_α remains the same as in the ideal case, S_β is now too a spherical cap with $r = r_\beta(\theta) = c_\beta \cos \theta + \sqrt{R_\beta^2 - c_\beta^2 \sin^2 \theta}$. By construction, the polar angle is still $\theta \in [\pi/2, \pi]$, and $\phi \in [0, 2\pi)$ as always. The normal to S_β is no longer a constant and is written $\mathbf{p}_0^\beta = (-\cos \theta + g_\beta(\theta) \sin^2 \theta, \sin \theta + g_\beta(\theta) \sin \theta \cos \theta, 0)$ with $g_\beta(\theta)$ defined analogously to equation (9).

Numerical details

We used the FEniCSx library DOLFINx [64] to implement the finite-element method in Python3. We minimised equation (2) in a 3D, symmetry-agnostic parameterisation for selected relevant parameters and observed that no spontaneous breaking of axial symmetry occurred. Thereafter, the mesh (with resolution 0.05) was parameterised in terms of r and θ only, corresponding to a constant- ϕ slice. We computed the variation of \mathcal{F} [equation (2)] with respect to the 3D vector OP \mathbf{p} in the direction of a test function φ to derive its weak formulation. The resulting non-linear problem was solved using a Newton solver with a relative tolerance of 10^{-6} .

Number and type of defects in the OP field were determined by visual inspection of the phase and direction of \mathbf{p} . Utilizing that $|\mathbf{p}| \rightarrow 0$ in the vicinity of defects due to the large local distortions they induce, we inferred the position of a defect as the central point of a mesh cell where $|\mathbf{p}| = 0$, surrounded by a region with $|\mathbf{p}| > 0$. The numerical uncertainty of these estimates thus depended on the size of the disordered region surrounding each defect and the resolution of the mesh. We defined a threshold p^* and checked in each cell whether $|\mathbf{p}| < p^*$. The value of p^* was fixed for each simulation, though we varied it conveniently from one to another in order to pre-select the least possible number of candidate points per defect (but in all cases, $p^* \leq 10^{-2}$). When more than one candidate points were selected, the location of the defect was calculated as the average of the candidate points. Error bars were determined as the standard deviation of their spatial distribution.

Culture and imaging of peri-implantation mouse embryos

To experimentally manipulate the tissue–tissue boundary in the peri-implantation mouse embryos, 3D-gel embedded embryo culture was performed as described in Ref. [37]. In brief, mouse embryos at embryonic day 4.5 were recovered from dissected uteri and cultured in a mixture of Matrigel–collagen I. Mural trophoctoderm (mTE) was microscurgically removed to enable polar trophoctoderm (pTE) invagination in the control condition, whereas maintaining mTE intact blocked pTE invagination and generated a boundary perturbation.

Embryos were fixed after 18 hours of culture with 4% paraformaldehyde (FUJIFILM Wako, 166-23251) in PBS for 30 minutes and subsequently permeabilised with 0.5% Triton X-100 (Nacalai, 12967-32) in PBS for 30 minutes. Embryos

were incubated in 3% BSA (Sigma, A9647) and 0.05% Triton X-100 in PBS overnight at 4°C and then subjected to immunostaining. Primary antibodies against Oct3/4 (Santa Cruz Biotechnology, sc-5279 AF647), Collagen IV (Millipore, AB756P), and pERM (Cell Signaling, 3726) were diluted at 1:100. Donkey anti-rabbit IgG Alexa Fluor Plus 488 (Invitrogen, A32790), DAPI (Invitrogen, D3571), and Alexa Fluor Plus 555 Phalloidin (Invitrogen, A30106) were simultaneously used at the secondary antibody staining.

Images were obtained by LSM880 or LSM980 equipped with a C-Apochromat 40x/1.2 NA water immersion objective (Zeiss).

Image analysis

The epiblast tissue marked by Oct3/4 positive cells was manually segmented with Napari [65]. Labels for the entire epiblast tissue area were drawn every 30 slices with 0.16 μm interval, followed by the plugin “napari-label-interpolator” to fill the entire volume. Then the label statistics function in the plugin “napari-simpleitk-image-processing” was used to count the number of voxels of the epiblast volume. We checked that perturbation of the tissue–tissue boundary introduced only geometric changes that preserved total volume. Indeed, average epiblast tissue volume was $(1.8 \pm 0.4) \times 10^5 \mu\text{m}^3$ in the manipulated cohort and $(2.3 \pm 0.4) \times 10^5 \mu\text{m}^3$ in the control condition.

Lumen position measurement was performed based on the space encircled with pERM signals with Fiji [66], using the middle cross-section, which was extracted by the 3D rotation function in Imaris (Bitplane).

Shape model fitting

Given the collections of points $\{(x_{\mu i}^{\text{exp}}, 0, z_{\mu i}^{\text{exp}})\}_{i=1, \dots, N_\mu}$ corresponding to the segmented tissue–tissue ($\mu = \alpha$) and tissue–ECM ($\mu = \beta$) contours, we identify the centroid of the epiblast and the two points \mathbf{b}_{left} , $\mathbf{b}_{\text{right}}$ where the different boundaries meet. We define the axis of symmetry as the line passing through the centroid and perpendicular to the line between \mathbf{b}_{left} and $\mathbf{b}_{\text{right}}$; the point where these lines intersect defines the origin of coordinates. After referring the contour points to this origin, we transform them to spherical coordinates, $\{(r_{\mu i}^{\text{exp}}, \theta_{\mu i}^{\text{exp}}, 0)\}_{i=1, \dots, N_\mu} = \{\mathbf{r}_{\mu i}^{\text{exp}}\}_{i=1, \dots, N_\mu} = \mathbf{r}_\mu^{\text{exp}}$, and minimise the cost function

$$h(\mathbf{r}_\alpha^{\text{exp}}, \mathbf{r}_\beta^{\text{exp}}; \kappa_\alpha, c_\alpha, \kappa_\beta, c_\beta) = \sum_{\mu=\alpha, \beta} \sum_{i=1}^{N_\mu} [\mathcal{R}(\mathbf{r}_{\mu i}^{\text{exp}}; \kappa_\mu, c_\mu)]^2. \quad (11)$$

Here,

$$\mathcal{R}(\mathbf{r}_{\mu i}^{\text{exp}}; \kappa_\mu, c_\mu) \equiv r_{\mu i}^{\text{exp}} - r(\theta_{\mu i}^{\text{exp}}; \kappa_\mu, c_\mu) \quad (12)$$

is the residual between the radius of experimental point i of boundary μ and the fitting function

$$r(\theta; \kappa_\mu, c_\mu) = c_\mu \cos \theta + \sqrt{1/\kappa_\mu^2 - c_\mu^2 \sin^2 \theta} \quad (13)$$

evaluated at that point, with $\kappa_\mu \equiv 1/R_\mu$ the curvature of the spherical cap and c_μ the z coordinate of its centre. To ensure continuity of the shape profile or, in other words, to guarantee a closed surface, we impose the constraint that

$r(\pi/2; \kappa_\alpha, c_\alpha) = r(\pi/2; \kappa_\beta, c_\beta)$ at the polar angle where, by construction, the two boundaries meet. Having found the best set $\tilde{\kappa}_\mu, \tilde{c}_\mu$, we calculate the acorn parameter

$$\nu_{\text{exp}} = \left(\tilde{c}_\alpha + \frac{s}{\tilde{\kappa}_\alpha} \right) \tilde{\kappa}_\beta, \quad (14)$$

where $s = 1$ ($s = -1$) if the tissue–tissue contour is convex (concave), and the base central angle

$$\sigma_{\text{exp}} = \cos^{-1}(-\tilde{c}_\beta \tilde{\kappa}_\beta) \quad (15)$$

that characterise the epiblast. Errors for the parameters are estimated by residual bootstrap. We generate a vector of residuals $\rho_\mu = (\delta r_{\mu 1}, \dots, \delta r_{\mu N_\mu})$, where $\delta r_{\mu i} = \mathcal{R}(\mathbf{r}_{\mu i}^{\text{exp}}; \tilde{\kappa}_\mu, \tilde{c}_\mu)$, for each boundary μ . A residual bootstrap sample $\rho'_\mu = (\delta r'_{\mu 1}, \dots, \delta r'_{\mu N_\mu})$ is generated by randomly selecting N_μ elements from ρ_μ with replacement. Then, the cost function (11) is evaluated at the modified datasets $\mathbf{r}_\mu^{\prime \text{exp}} = \{ (r(\theta_{\mu i}^{\text{exp}}; \tilde{\kappa}_\mu, \tilde{c}_\mu) + \delta r'_{\mu i}, \theta_{\mu i}^{\text{exp}}, 0) \}_{i=1, \dots, N_\mu}$ and minimised to obtain the corresponding best set of parameters. We repeat this process for 100 residual bootstrap samples to generate distributions of the fitting parameters, and use their standard deviation as uncertainties $\Delta \tilde{\kappa}_\mu, \Delta \tilde{c}_\mu$. These give rise to

$$\Delta \nu_{\text{exp}} = \sqrt{\tilde{\kappa}_\beta^2 \Delta \tilde{c}_\alpha^2 + \frac{\tilde{\kappa}_\beta^2}{\tilde{\kappa}_\alpha^4} \Delta \tilde{\kappa}_\alpha^2 + \frac{\nu_{\text{exp}}^2}{\tilde{\kappa}_\beta^2} \Delta \tilde{\kappa}_\beta^2} \quad (16)$$

and

$$\Delta \sigma_{\text{exp}} = \sqrt{\frac{\tilde{\kappa}_\beta^2 \Delta \tilde{c}_\beta^2 + \tilde{c}_\beta^2 \Delta \tilde{\kappa}_\beta^2}{1 - \tilde{c}_\beta^2 \tilde{\kappa}_\beta^2}}. \quad (17)$$

REFERENCES

- [1] N. A. Araújo, L. M. Janssen, T. Barois, G. Boffetta, I. Cohen, A. Corbetta, O. Dauchot, M. Dijkstra, W. M. Durham, A. Dussutour, *et al.*, “Steering self-organisation through confinement,” *Soft Matter* **19**, 1695–1704 (2023).
- [2] L. C. Bradley, W.-H. Chen, K. J. Stebe, and D. Lee, “Janus and patchy colloids at fluid interfaces,” *Current Opinion in Colloid & Interface Science* **30**, 25–33 (2017).
- [3] A. Trushko, I. Di Meglio, A. Merzouki, C. Blanch-Mercader, S. Abuhattum, J. Guck, K. Alessandri, P. Nassoy, K. Kruse, B. Chopard, *et al.*, “Buckling of an epithelium growing under spherical confinement,” *Developmental Cell* **54**, 655–668 (2020).
- [4] S. Harmansa, A. Erlich, C. Eloy, G. Zurlo, and T. Lecuit, “Growth anisotropy of the extracellular matrix shapes a developing organ,” *Nature Communications* **14**, 1220 (2023).
- [5] T. Lopez-Leon and A. Fernandez-Nieves, “Drops and shells of liquid crystal,” *Colloid and Polymer Science* **289**, 345–359 (2011).
- [6] A. Sieben, J. Schumann, and A. Seyfried, “Collective phenomena in crowds—where pedestrian dynamics need social psychology,” *PLoS one* **12**, e0177328 (2017).
- [7] J.-L. Barrat, E. Del Gado, S. U. Egelhaaf, X. Mao, M. Dijkstra, D. J. Pine, S. K. Kumar, K. Bishop, O. Gang, A. Obermeyer, *et al.*, “Soft matter roadmap,” *Journal of Physics: Materials* **7**, 012501 (2023).
- [8] I. Nys, “Patterned surface alignment to create complex three-dimensional nematic and chiral nematic liquid crystal structures,” *Liquid Crystals Today* **29**, 65–83 (2020).
- [9] M. Daëff, “Confined particles in microfluidic devices: a review,” *Elveflow* (2020).

- [10] H. Xin, H. Chen, P. Song, and Q. Sun, “Alignment control of thermotropic liquid crystals by topography and chemical functionality of a surface: a review,” [Materials Today Communications](#) , 106680 (2023).
- [11] P. Sheng, “Phase transition in surface-aligned nematic films,” [Physical Review Letters](#) **37**, 1059 (1976).
- [12] P. Sheng, “Boundary-layer phase transition in nematic liquid crystals,” [Physical Review A](#) **26**, 1610 (1982).
- [13] G. Crawford, R. Stannarius, and J. Doane, “Surface-induced orientational order in the isotropic phase of a liquid-crystal material,” [Physical Review A](#) **44**, 2558 (1991).
- [14] J. Nijjer, C. Li, M. Kothari, T. Henzel, Q. Zhang, J.-S. B. Tai, S. Zhou, T. Cohen, S. Zhang, and J. Yan, “Biofilms as self-shaping growing nematics,” [Nature Physics](#) , 1–9 (2023).
- [15] V. Bondarenko, M. Nikolaev, D. Kromm, R. Belousov, A. Wolny, M. Blotenburg, P. Zeller, S. Rezakhani, J. Hugger, V. Uhlmann, *et al.*, “Embryo-uterine interaction coordinates mouse embryogenesis during implantation,” [The EMBO Journal](#) , e113280 (2023).
- [16] L. E. O’Brien, T.-S. Jou, A. L. Pollack, Q. Zhang, S. H. Hansen, P. Yurchenco, and K. E. Mostov, “Rac1 orientates epithelial apical polarity through effects on basolateral laminin assembly,” [Nature Cell Biology](#) **3**, 831–838 (2001).
- [17] N. Akhtar and C. H. Streuli, “An integrin–ILK–microtubule network orients cell polarity and lumen formation in glandular epithelium,” [Nature Cell Biology](#) **15**, 17–27 (2013).
- [18] J. P. Rasmussen, S. S. Reddy, and J. R. Priess, “Laminin is required to orient epithelial polarity in the *C. elegans* pharynx,” [Development](#) **139**, 2050–2060 (2012).
- [19] C. F. Davey and C. B. Moens, “Planar cell polarity in moving cells: think globally, act locally,” [Development](#) **144**, 187–200 (2017).
- [20] M. T. Butler and J. B. Wallingford, “Planar cell polarity in development and disease,” [Nature Reviews Molecular Cell Biology](#) **18**, 375–388 (2017).
- [21] B. Ladoux, R.-M. Mège, and X. Trepat, “Front–rear polarization by mechanical cues: from single cells to tissues,” [Trends in Cell Biology](#) **26**, 420–433 (2016).
- [22] K. H. Palmquist, S. F. Tiemann, F. L. Ezzeddine, S. Yang, C. R. Pfeifer, A. Erzberger, A. R. Rodrigues, and A. E. Shyer, “Reciprocal cell-ECM dynamics generate supracellular fluidity underlying spontaneous follicle patterning,” [Cell](#) **185**, 1960–1973 (2022).
- [23] F. N. Vicente and A. Diz-Muñoz, “Order from chaos: how mechanics shape epithelia and promote self-organization,” [Current Opinion in Systems Biology](#) , 100446 (2023).
- [24] C. E. Buckley and D. St Johnston, “Apical–basal polarity and the control of epithelial form and function,” [Nature Reviews Molecular Cell biology](#) **23**, 559–577 (2022).
- [25] R. Ienaga, K. Beppu, and Y. T. Maeda, “Geometric confinement guides topological defect pairings and emergent flow in nematic cell populations,” [Soft Matter](#) **19**, 5016–5028 (2023).
- [26] F. Vafa, D. R. Nelson, and A. Doostmohammadi, “Periodic orbits, pair nucleation, and unbinding of active nematic defects on cones,” [arXiv preprint arXiv:2310.06022](#) (2023).
- [27] A. Ardaševa and A. Doostmohammadi, “Topological defects in biological matter,” [Nature Reviews Physics](#) **4**, 354–356 (2022).
- [28] K. Copenhagen, R. Alert, N. S. Wingreen, and J. W. Shaevitz, “Topological defects promote layer formation in *Myxococcus xanthus* colonies,” [Nature Physics](#) **17**, 211–215 (2021).
- [29] Y. Maroudas-Sacks, L. Garion, L. Shani-Zerbib, A. Livshits, E. Braun, and K. Keren, “Topological defects in the nematic order of actin fibres as organization centres of hydra morphogenesis,” [Nature Physics](#) **17**, 251–259 (2021).
- [30] H. Li, X.-q. Shi, M. Huang, X. Chen, M. Xiao, C. Liu, H. Chaté, and H. Zhang, “Data-driven quantitative modeling of bacterial active nematics,” [Proceedings of the National Academy of Sciences](#) **116**, 777–785 (2019).

- [31] Y. I. Yaman, E. Demir, R. Vetter, and A. Kocabas, “Emergence of active nematics in chaining bacterial biofilms,” [Nature Communications](#) **10**, 2285 (2019).
- [32] K. Kawaguchi, R. Kageyama, and M. Sano, “Topological defects control collective dynamics in neural progenitor cell cultures,” [Nature](#) **545**, 327–331 (2017).
- [33] T. B. Saw, A. Doostmohammadi, V. Nier, L. Kocgozlu, S. Thampi, Y. Toyama, P. Marcq, C. T. Lim, J. M. Yeomans, and B. Ladoux, “Topological defects in epithelia govern cell death and extrusion,” [Nature](#) **544**, 212–216 (2017).
- [34] C. Blanch-Mercader, V. Yashunsky, S. Garcia, G. Duclos, L. Giomi, and P. Silberzan, “Turbulent dynamics of epithelial cell cultures,” [Physical Review Letters](#) **120**, 208101 (2018).
- [35] C. Blanch-Mercader, P. Guillamat, A. Roux, and K. Kruse, “Integer topological defects of cell monolayers: mechanics and flows,” [Physical Review E](#) **103**, 012405 (2021).
- [36] C. Blanch-Mercader, P. Guillamat, A. Roux, and K. Kruse, “Quantifying material properties of cell monolayers by analyzing integer topological defects,” [Physical Review Letters](#) **126**, 028101 (2021).
- [37] T. Ichikawa, H. T. Zhang, L. Panavaite, A. Erzberger, D. Fabrèges, R. Snajder, A. Wolny, E. Korotkevich, N. Tsuchida-Straeten, L. Hufnagel, *et al.*, “An ex vivo system to study cellular dynamics underlying mouse peri-implantation development,” [Developmental Cell](#) **57**, 373–386 (2022).
- [38] I. Bedzhov and M. Zernicka-Goetz, “Self-organizing properties of mouse pluripotent cells initiate morphogenesis upon implantation,” [Cell](#) **156**, 1032–1044 (2014).
- [39] F. Jülicher, S. W. Grill, and G. Salbreux, “Hydrodynamic theory of active matter,” [Reports on Progress in Physics](#) **81**, 076601 (2018).
- [40] P.-G. De Gennes, “Short range order effects in the isotropic phase of nematics and cholesterics,” [Molecular Crystals and Liquid Crystals](#) **12**, 193–214 (1971).
- [41] P. Prinsen and P. Van Der Schoot, “Shape and director-field transformation of tactoids,” [Physical Review E](#) **68**, 021701 (2003).
- [42] S. R. Seyednejad, M. R. Mozaffari, and M. R. Ejtehad, “Confined nematic liquid crystal between two spherical boundaries with planar anchoring,” [Physical Review E](#) **88**, 012508 (2013).
- [43] A. Mertelj and D. Lisjak, “Ferromagnetic nematic liquid crystals,” [Liquid Crystals Reviews](#) **5**, 1–33 (2017).
- [44] O. Prishchepa, A. Shabanov, and V. Y. Zyryanov, “Director configurations in nematic droplets with inhomogeneous boundary conditions,” [Physical Review E](#) **72**, 031712 (2005).
- [45] M. Ravnik and S. Žumer, “Landau–de gennes modelling of nematic liquid crystal colloids,” [Liquid Crystals](#) **36**, 1201–1214 (2009).
- [46] L. Tran, M. O. Lavrentovich, D. A. Beller, N. Li, K. J. Stebe, and R. D. Kamien, “Lassoing saddle splay and the geometrical control of topological defects,” [Proceedings of the National Academy of Sciences](#) **113**, 7106–7111 (2016).
- [47] M. A. Molè, A. Weberling, R. Fässler, A. Campbell, S. Fishel, and M. Zernicka-Goetz, “Integrin $\beta 1$ coordinates survival and morphogenesis of the embryonic lineage upon implantation and pluripotency transition,” [Cell Reports](#) **34** (2021), 10.1016/j.celrep.2021.108834.
- [48] D. Revignas and A. Ferrarini, “Interplay of particle morphology and director distortions in nematic fluids,” [Physical Review Letters](#) **125**, 267802 (2020).
- [49] O. D. Lavrentovich, “Splay-bend elastic inequalities shape tactoids, toroids, umbilics, and conic section walls in paraelectric, twist-bend, and ferroelectric nematics,” [Liquid Crystals Reviews](#) **12**, 1–13 (2024).
- [50] A. Mietke, V. Jemseena, K. V. Kumar, I. F. Sbalzarini, and F. Jülicher, “Minimal model of cellular symmetry breaking,” [Physical Review Letters](#) **123**, 188101 (2019).
- [51] G. Volovik and O. Lavrentovich, “Topological dynamics of defects: boojums in nematic drops,” [Journal of Experimental and Theoretical Physics](#) **85**, 1997–2010 (1983).

- [52] J. Pollard and R. G. Morris, “Morse theory and meron mediated interactions between disclination lines in nematics,” [arXiv preprint arXiv:2408.01032](#) (2024).
- [53] S. Mkaddem and E. Gartland Jr, “Fine structure of defects in radial nematic droplets,” [Physical Review E](#) **62**, 6694 (2000).
- [54] L. A. Hoffmann, L. N. Carenza, J. Eckert, and L. Giori, “Theory of defect-mediated morphogenesis,” [Science Advances](#) **8**, eabk2712 (2022).
- [55] S. M. Paul, M. Ternet, P. M. Salvaterra, and G. J. Beitel, “The Na⁺/K⁺ ATPase is required for septate junction function and epithelial tube-size control in the Drosophila tracheal system,” [Development](#) **130**, 4963–4974 (2003).
- [56] L. Rathbun, E. Colicino, J. Manikas, J. O’Connell, N. Krishnan, N. Reilly, S. Coyne, G. Erdemci-Tandogan, A. Garrastegui, J. Freshour, *et al.*, “Cytokinetic bridge triggers de novo lumen formation in vivo,” [Nature Communications](#) **11**, 1269 (2020).
- [57] D. M. Bryant, A. Datta, A. E. Rodríguez-Fraticelli, J. Peränen, F. Martín-Belmonte, and K. E. Mostov, “A molecular network for de novo generation of the apical surface and lumen,” [Nature Cell Biology](#) **12**, 1035–1045 (2010).
- [58] S. Sigurbjörnsdóttir, R. Mathew, and M. Leptin, “Molecular mechanisms of de novo lumen formation,” [Nature Reviews Molecular Cell biology](#) **15**, 665–676 (2014).
- [59] N. Christodoulou, A. Weberling, D. Strathdee, K. I. Anderson, P. Timpson, and M. Zernicka-Goetz, “Morphogenesis of extra-embryonic tissues directs the remodelling of the mouse embryo at implantation,” [Nature Communications](#) **10**, 3557 (2019).
- [60] P. Guillamat, C. Blanch-Mercader, G. Pernollet, K. Kruse, and A. Roux, “Integer topological defects organize stresses driving tissue morphogenesis,” [Nature Materials](#) **21**, 588–597 (2022).
- [61] S. Durdu, M. Iskar, C. Revenu, N. Schieber, A. Kunze, P. Bork, Y. Schwab, and D. Gilmour, “Luminal signalling links cell communication to tissue architecture during organogenesis,” [Nature](#) **515**, 120–124 (2014).
- [62] A. Q. Ryan, C. J. Chan, F. Graner, and T. Hiiragi, “Lumen expansion facilitates epiblast-primitive endoderm fate specification during mouse blastocyst formation,” [Developmental Cell](#) **51**, 684–697 (2019).
- [63] Y. S. Kim, R. Fan, L. Kremer, N. Kuempel-Rink, K. Mildner, D. Zeuschner, L. Hekking, M. Stehling, and I. Bedzhov, “Deciphering epiblast lumenogenesis reveals proamniotic cavity control of embryo growth and patterning,” [Science Advances](#) **7**, eabe1640 (2021).
- [64] M. W. Scroggs, J. S. Dokken, C. N. Richardson, and G. N. Wells, “Construction of arbitrary order finite element degree-of-freedom maps on polygonal and polyhedral cell meshes,” [ACM Transactions on Mathematical Software](#) **48** (2022), 10.1145/3524456.
- [65] J. Ahlers, D. Althviz Moré, O. Amsalem, A. Anderson, G. Bokota, P. Boone, J. a. Bragantini, G. Buckley, A. Burt, M. Bussonnier, *et al.*, “[napari: a multi-dimensional image viewer for Python](#),” (2023).
- [66] J. Schindelin, I. Arganda-Carreras, E. Frise, V. Kaynig, M. Longair, T. Pietzsch, S. Preibisch, C. Rueden, S. Saalfeld, B. Schmid, *et al.*, “Fiji: an open-source platform for biological-image analysis,” [Nature Methods](#) **9**, 676–682 (2012).

DATA AVAILABILITY

The data that support the findings of this study will be made public upon publication.

CODE AVAILABILITY

All the codes that support this study are available at <https://git.embl.de/guruciag/geometry-driven-defects>.

ACKNOWLEDGEMENTS

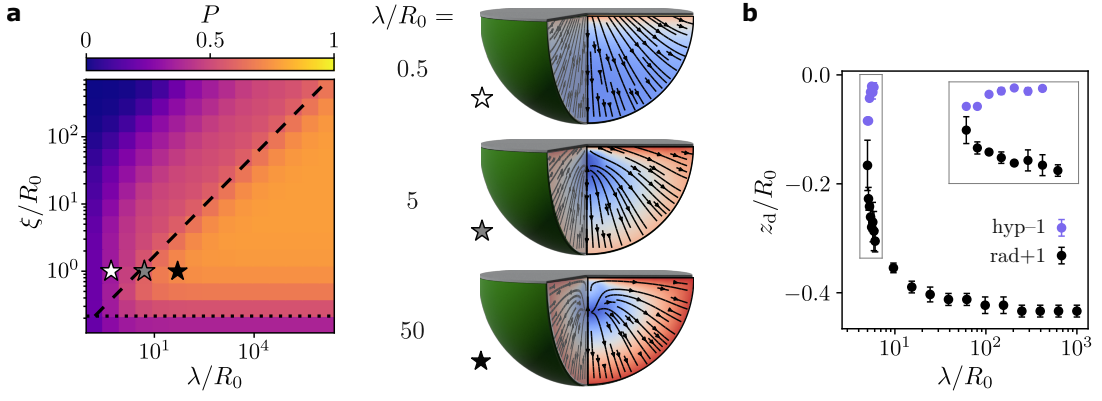
We thank R. Belousov, V. Bondarenko, T. Dullweber, J. Ellenberg, J. Elliott, I. Estabrook, P. Jentsch, L. Manning, C. Modes, T. Quail, J. Rombouts, and A. Torres Sánchez for useful discussions and valuable feedback on the manuscript. The Erzberger group is funded by the EMBL. The Hiiragi laboratory was supported by the EMBL, and currently by the Hubrecht Institute, the European Research Council (ERC Advanced Grant “SelforganisingEmbryo” grant agreement 742732, ERC Advanced Grant “COORDINATION” grant agreement 101055287), Stichting LSH-TKI (LSHM21020), and Japan Society for the Promotion of Science (JSPS) KAKENHI grant numbers JP21H05038 and JP22H05166. P.C.G. is supported by the EMBL Interdisciplinary Postdoctoral Fellowship (EIPOD4) programme under Marie Skłodowska-Curie Actions Cofund (grant agreement 847543), and by an Add-on Fellowship for Interdisciplinary Life Science of the Joachim Herz Stiftung. P.C.G. thanks Kyoto University for its hospitality during part of the preparation of this work.

AUTHOR CONTRIBUTIONS

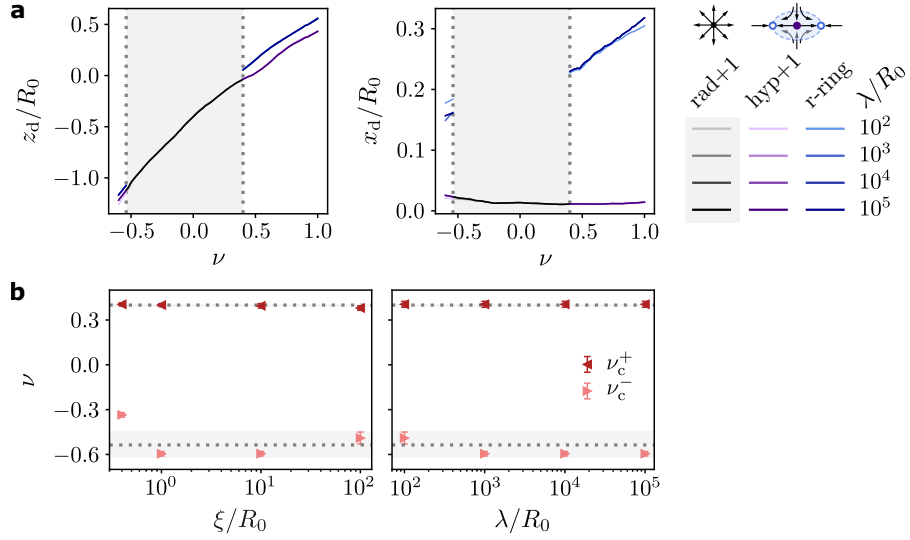
All authors designed the research. P.C.G. performed the numerical work. T.I. performed the experiments. T.I. and P.C.G. analysed the data and fitted the shape model. P.C.G. prepared the figures with input from A.E. P.C.G. and A.E. wrote the paper with contributions from T.I. and T.H.

COMPETING INTERESTS

The authors declare no competing interests.

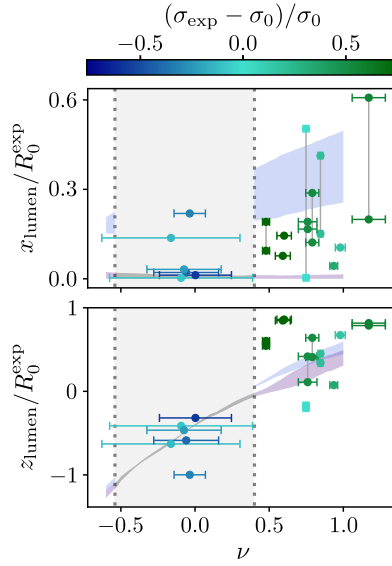


Extended Data FIG. 1. **The degree of global order and type of defects depend on the confining geometry.** **a**, Global degree of order P [equation (1)] of a hemispherical system with mixed \mathbf{p}_0 . Order penetrates into the bulk more easily than in spherical confinement, obtaining $P > 0.5$ in the limit $\lambda \rightarrow \infty$ for $\xi > 0.2R_0$ (dotted line). Stars denote the parameter values for example field configurations, where defects are created in order to accommodate the increasingly relevant boundary conditions ($\xi/R_0 = 1$, $k_0/k_2 = 10$). The value $\zeta^* \approx 0.3R_0$ (dashed line) that separates defect-free and defect-containing configurations is independent of the confining geometry. **b**, Increasing the anchoring length λ changes the defect height z_d ($\xi/R_0 = 1$, $k_0/k_2 = 10$). The hyp-1 bulk defect moves up and becomes a hyperbolic boojum on the surface, leaving behind only the rad+1 hedgehog. Points and error bars correspond to the mean and standard deviation of the position of the defect candidates (see [Methods](#)). The vertical dashed line marks the value $\lambda^* = \xi^2/\zeta^*$.



Extended Data FIG. 2. **The position of defects and the transitions between them are robust to parameter changes.**

a, Within the highly ordered regime, the location of the defects is not affected by a three order of magnitude variation of the anchoring length ($\xi/R_0 = 1$, $k_0/k_2 = 10$). **b**, The critical values of the acorn parameter where the transitions between defect configurations occur remain unchanged under variation of the mechanical parameters, giving $\nu_c^+ = 0.400 \pm 0.008$ and $\nu_c^- = -0.54 \pm 0.09$ (dotted lines and shaded area).



Extended Data FIG. 3. **Lumina vs. generalised-acorn parameters of the studied epiblasts.** Lumen centroid positions in terms of the individually fitted parameters of the generalised acorn model, ν_{exp} and σ_{exp} . The color map represents the relative deviation from the ideal acorn shape, characterised by $\sigma_0 = \pi/2$. Coloured shaded regions show the defect position ranges for ideal acorns with $\lambda/R_0 = 10^6$, $\xi/R_0 \in [0.4, 100]$ and $k_0/k_2 = 10$. The volume V_0^{exp} of the epiblast tissue defines $R_0^{\text{exp}} = (3V_0^{\text{exp}}/4\pi)^{1/3}$ for each embryo. Error bars are determined by residual bootstrapping of the epiblast boundaries (see [Methods](#)).

SUPPLEMENTARY NOTE

Derivation of the Euler-Lagrange equations

In order to find the value of the vector field $\mathbf{p}(\mathbf{r})$ that minimises the free energy functional

$$\mathcal{F}[\mathbf{p}] = \int_{\Omega} dV f_{\text{B}}(\mathbf{p}, \nabla \mathbf{p}) + \int_{\partial\Omega} dS f_{\text{S}}(\mathbf{p}), \quad (1)$$

in a volume Ω , we write the variation

$$\delta\mathcal{F} = \int_{\Omega} dV \left[\frac{\partial f_{\text{B}}}{\partial p_i} \delta p_i + \frac{\partial f_{\text{B}}}{\partial (\nabla p_i)} \cdot \nabla (\delta p_i) \right] + \int_{\partial\Omega} dS \frac{\partial f_{\text{S}}}{\partial p_i} \delta p_i, \quad (2)$$

where Einstein summation convention over repeated indexes is used. The second term of the volume integral can be integrated by parts to yield

$$\begin{aligned} \int_{\Omega} dV \frac{\partial f_{\text{B}}}{\partial (\nabla p_i)} \cdot \nabla (\delta p_i) &= \int_{\Omega} dV \left\{ -\nabla \cdot \left[\frac{\partial f_{\text{B}}}{\partial (\nabla p_i)} \right] \delta p_i + \nabla \cdot \left[\frac{\partial f_{\text{B}}}{\partial (\nabla p_i)} \delta p_i \right] \right\} \\ &= - \int_{\Omega} dV \nabla \cdot \left[\frac{\partial f_{\text{B}}}{\partial (\nabla p_i)} \right] \delta p_i + \int_{\partial\Omega} dS \hat{\mathbf{n}} \cdot \frac{\partial f_{\text{B}}}{\partial (\nabla p_i)} \delta p_i \end{aligned} \quad (3)$$

with $\hat{\mathbf{n}}$ the outward normal. Thus, equation (2) becomes

$$\delta\mathcal{F} = \int_{\Omega} dV \left[\frac{\partial f_{\text{B}}}{\partial p_i} - \nabla \cdot \frac{\partial f_{\text{B}}}{\partial (\nabla p_i)} \right] \delta p_i + \int_{\partial\Omega} dS \left[\frac{\partial f_{\text{S}}}{\partial p_i} + \hat{\mathbf{n}} \cdot \frac{\partial f_{\text{B}}}{\partial (\nabla p_i)} \right] \delta p_i. \quad (4)$$

If the minimising field \mathbf{p} were to have a fixed value on the boundary (essential boundary conditions), $\delta p_i|_{\partial\Omega} = 0$ and the surface integral would vanish directly. In our case, however, we take boundary conditions on \mathbf{p} to be natural, meaning that they are not imposed externally, but are *naturally* derived from the problem and satisfied after a solution has been found. Hence, for arbitrary variations δp_i , we enforce

$$\frac{\partial f_{\text{S}}}{\partial p_i} + \hat{\mathbf{n}} \cdot \frac{\partial f_{\text{B}}}{\partial (\nabla p_i)} = 0 \quad \text{in } \partial\Omega. \quad (5)$$

These equations ensure continuity of \mathbf{p} on the surface and leave us only with the volume integral. Finally, asking that $\delta\mathcal{F} = 0$ gives rise to the set of coupled partial differential equations

$$\frac{\partial f_{\text{B}}}{\partial p_i} - \nabla \cdot \frac{\partial f_{\text{B}}}{\partial (\nabla p_i)} = 0 \quad \text{in } \Omega, \quad (6)$$

which are the Euler-Lagrange equations of the problem.